Asian Journal of Pharmaceutical Sciences 18 (2023) 100798

Available online at www.sciencedirect.com

ScienceDirect

journal homepage: www.elsevier.com/locate/AJPS

Original Research Paper

# Tumor microenvironment-responsive artesunate loaded Z-scheme heterostructures for synergistic photo-chemodynamic therapy of hypoxic tumor

*Jie Lv*[a,b], *Xiaoyu Wang*[a], *Xue Zhang*[a], *Runpei Xu*[a], *Shuyang Hu*[a], *Shuangling Wang*[a], *Meng Li*[a,*]

[a] *College of Pharmacy, Key Laboratory of Innovative Drug Development and Evaluation, Hebei Medical University, Shijiazhuang 050017, China*

[b] *Postdoctoral Mobile Station of Basic Medicine, Hebei Medical University, Shijiazhuang 050017, China*

ARTICLE INFO

*Article history:*
Received 28 November 2022
Revised 15 February 2023
Accepted 26 February 2023
Available online 20 March 2023

*Keywords:*
Hypoxia
Z-scheme heterostructure
Artesunate
Tumor microenvironment
Glutathione peroxidase 4
Synergistic therapy

ABSTRACT

Tumor microenvironment (TME) with the particular features of severe hypoxia, insufficient endogenous $H_2O_2$, and overexpression of glutathione (GSH) markedly reduced the antitumor efficacy of monotherapy. Herein, a TME-responsive multifunctional nanoplatform ($Bi_2S_3$@Bi@PDA-HA/Art NRs) was presented for synergistic photothermal therapy (PTT), chemodynamic therapy (CDT), and photodynamic therapy (PDT) to achieve better therapeutic outcomes. The Z-scheme heterostructured bismuth sulfide@bismuth nanorods ($Bi_2S_3$@Bi NRs) guaranteed excellent photothermal performance of the nanoplatform. Moreover, its ability to produce $O_2$ and reactive oxygen species (ROS) synchronously could relieve tumor hypoxia and improve PDT outcomes. The densely coated polydopamine/ammonium bicarbonate (PDA/ABC) and hyaluronic acid (HA) layers on the surface of the nanoplatform enhanced the cancer-targeting capacity and induced the acidic TME-triggered *in situ* "bomb-like" release of Art. The CDT treatment was achieved by activating the released Art through intracellular $Fe^{2+}$ ions in an $H_2O_2$-independent manner. Furthermore, decreasing the glutathione peroxidase 4 (GPX4) levels by Art could also increase the PDT efficiency of $Bi_2S_3$@Bi NRs. Owing to the synergistic effect, this nanoplatform displayed improved antitumor efficacy with minimal toxicity both *in vitro* and *in vivo*. Our design sheds light on the application of phototherapy combined with the traditional Chinese medicine monomer-artesunate in treating the hypoxic tumor.



* Corresponding author.
*E-mail address:* limeng87@hotmail.com (M. Li).
Peer review under responsibility of Shenyang Pharmaceutical University.

https://doi.org/10.1016/j.ajps.2023.100798

## 1. Introduction

Photodynamic therapy (PDT) has been regarded as an attractive oncotherapy due to its noninvasive nature, low systemic toxicity, and spatio-temporal controllability [1–3]. Although promising, PDT's $O_2$ dependence limits its therapeutic efficacy in hypoxic solid tumors [4,5]. To address this issue, some strategies for overcoming tumorous hypoxia have been proposed, such as using an intelligent nanoplatform to transport $O_2$ to tumor sites or decomposing endogenous hydrogen peroxide ($H_2O_2$) for *in situ* generation of $O_2$ within solid tumors [6].

Indeed, $O_2$ carriers including hemoglobin and perfluorocarbon can deliver $O_2$ to tumor sites [7] as well as catalase (CAT) or CAT-like nanomaterials such as manganese dioxide ($MnO_2$)-containing nanostructures, platinum-based nanoparticles and gold nanoclusters which serve as *in situ* $O_2$ generators, have been widely investigated to improve PDT efficiency by increasing intratumoral $O_2$ supply [8–11]. However, the low $O_2$-carrying capacity, particularly the uncontrollable and unexpected release behavior, severely limits the use of these nanocarriers [11], while the low intracellular $H_2O_2$ level results in insufficient $O_2$ production by CAT or CAT-mimic nanozymes [12–14]. On the other hand, for a viable PDT system, additional photosensitizers (PSs) must be introduced in addition to these $O_2$ donors. The asynchronous nature of $O_2$ supplements and the formation of reactive oxygen species (ROS) in these systems still resulted in unsatisfactory PDT efficacy [15]. Hence, developing a novel therapeutic nanoplatform capable of achieving spatiotemporally synchronous $O_2$ self-supply and ROS production under near-infrared (NIR) laser irradiation remains a desirable goal for PDT in hypoxic tumor treatment.

Recently, bismuth sulfide-based nanomaterials ($Bi_2S_3$ NMs) with NIR-responsive photocatalytic activity have been identified as promising PDT agents. However, the low electron mobility and rapid hole-electron recombination give rise to a low ROS production capability of these reported $Bi_2S_3$ NMs. Intriguingly, the photodynamic performance of $Bi_2S_3$ NMs can be significantly improved by forming heterostructures especially Z-scheme heterostructures with other materials [16]. Z-scheme heterostructure materials which are composed of two different semiconductors (PS I and PS II) and solid electronic mediator, not only effectively achieve the spatial separation of electron-hole pairs, but also remain the strong oxidation–reduction active sites, directly leading to the improved efficiency of ROS generation under irradiation [17]. Moreover, the high NIR absorption coefficient of $Bi_2S_3$ NMs endows them with an excellent photothermal effect, which can also be enhanced by the formation of Z-scheme heterostructures. The enhanced photothermal effect would further improve their photocatalytic efficiency [18]. Based on this concept, the Z-scheme heterostructured $Bi_2S_3$@bismuth nanorods ($Bi_2S_3$@Bi NRs) were designed [18]. Besides the excellent PDT performance, the hole in the valence band of $Bi_2S_3$ can react with $H_2O_2$ to produce $O_2$ upon NIR irradiation. Meanwhile, the electron in the conduction band of Bi reacts with $O_2$ to generate ROS [18,19], endowing the $Bi_2S_3$@Bi NRs with the ability to self-supply $O_2$ and produce ROS in an $H_2O_2$-independent and spatiotemporally synchronous manner to alleviate tumor hypoxia for enhanced PDT.

In the present study, a tumor microenvironment (TME)-responsive multifunctional nanoplatform denoted as $Bi_2S_3$@Bi@PDA-HA/Art NRs was rationally designed by combining artesunate (Art) with Z-scheme heterostructured $Bi_2S_3$@Bi NRs, which integrated the functions of tumor targeting, photothermal therapy (PTT), chemodynamic therapy (CDT) and PDT to maximize the therapeutic effect against hypoxic tumor (Scheme 1). Art, a class of endoperoxide-containing sesquiterpene extracted from the Chinese herb *Artemisia annua*, can promote transferrin to degrade into $Fe^{2+}$ ions, leading to the overexpression of $Fe^{2+}$ ions in tumor cells [20]. Then Art can be activated by overexpressed intracellular $Fe^{2+}$ ions to generate ROS and thus achieve efficient $H_2O_2$-independent CDT treatment [21]. Importantly, Art has been reported to have the ability to consume intracellular glutathione (GSH) and decrease the glutathione peroxidase 4 (GPX4) levels [22,23], which can significantly improve the PDT efficiency of $Bi_2S_3$@Bi NRs. The self-coating polydopamine/ammonium bicarbonate (PDA/ABC) layer on the surface of the $Bi_2S_3$@Bi NRs served as a pH-sensitive substrate for loading Art [24]. The cancer-targeting capacity of the nanoplatform could be enhanced by hyaluronic acid (HA) modification [25]. Moreover, NIR irradiation generated a large amount of $O_2$ and ROS synchronously and produced local heat due to the high NIR photothermal conversion efficiency of $Bi_2S_3$@Bi NRs and the PDA shell, resulting in relieving tumor hypoxia and a synergistic effect of PTT/PDT. Meanwhile, the generated local heat triggered the decomposition of ABC, which in turn aggravated the damage of the PDA shell and accelerated the release of Art. Owing to the selective accumulation in cancer cells and the localized therapeutic effects of PTT, CDT and Art-assisted PDT, the nanoplatform showed multi-amplified antitumor effects with negligible systemic toxicity both *in vitro* and *in vivo*.

## 2. Materials and methods

### 2.1. Materials

Oleylamine, oleic acid (OA), Tween-20, dopamine hydrochloride (DA·HCl), tris(hydroxymethyl)aminomethane (tris), hydrazinium hydrate, thioacetamide, and artesunate (Art) were obtained from Aladdin. Bismuth neodecanoate and 4′,6-diamidino-2-phenylindole (DAPI) were purchased from Sigma–Aldrich. Ammonium bicarbonate ($NH_4HCO_3$, ABC) was bought from Tianjin Yongda Chemical Reagent Technology Co., Ltd. $[Ru(dpp)_3]Cl_2$ (RDPP) was purchased from J&K Scientific. GSH and GSSG Assay Kit, Lyso-Tracker Red, and 2′,7′ -dichlorofluorescein diacetate (DCFH-DA) were bought from Beyotime Biotechnology. Hyaluronic acid (HA) was obtained from Shanghai Macklin Biochemical Technology Co., Ltd. Pimonidazole hydrochloride was purchased from Med Chem Express. Live and dead cell staining kit was obtained from Biovision. Glutathione peroxidase 4 (GPX4) ELISA Kit was bought from Shanghai Jianglai industrial limited by Share Ltd. Deionized water (D.I. water) was produced to prepare all

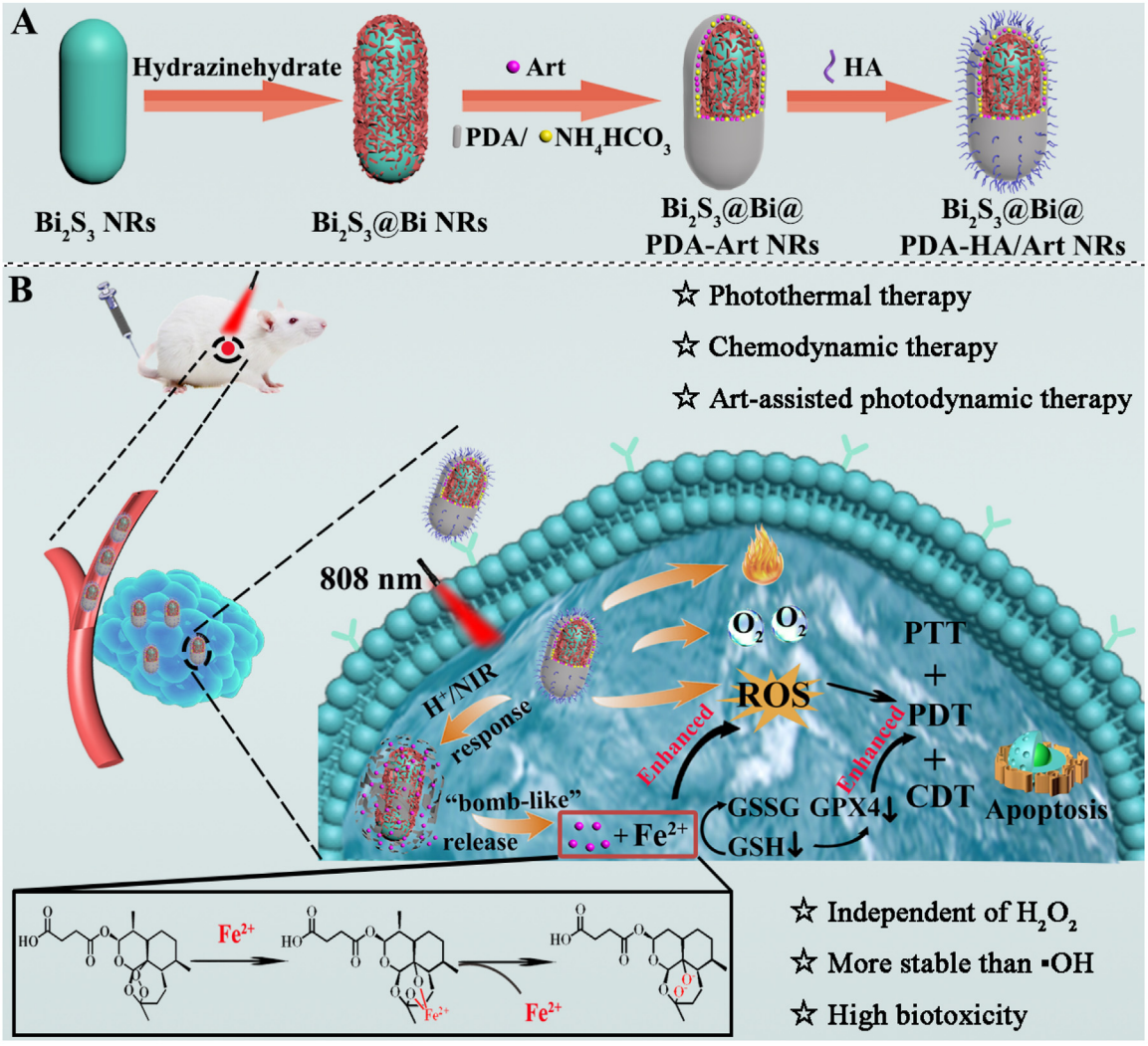


**Scheme 1 – Schematic illustration of the preparation and therapeutic functions of $Bi_2S_3$@Bi@PDA-HA/Art NRs.**

solutions. All the reagents (analytical grade) were directly used as received.

### 2.2. *Preparation of $Bi_2S_3$@Bi NRs*

The $Bi_2S_3$ NRs were first synthesized by the solvothermal method according to the previous reports [26,27]. The $Bi_2S_3$@Bi NRs were obtained through *in situ* reduction of $Bi^{3+}$ on the surface of $Bi_2S_3$ NRs. Briefly, 50 mg Tween-20 coated $Bi_2S_3$ NRs was uniformly dispersed in 9 ml D.I. water, and then 1 ml NaOH (1 M) aqueous solution and 0.5 ml hydrazine hydrate (50%) were added into this solution. After 1 h of mixing, the obtained solution was placed into a 20 ml Teflon-lined stainless-steel autoclave and treated for 3 h at 150 °C. The final product-$Bi_2S_3$@Bi NRs was obtained by centrifuging at 10,000 rpm for 5 min, washing with D.I. water 3 times, and drying under vacuum at 60 °C overnight in turn.

### 2.3. *Preparation of $Bi_2S_3$@Bi@PDA NRs*

10 mg $Bi_2S_3$@Bi NRs was sonicated and dispersed in 100 ml 10 mM tris solution containing 1 mg DA·HCl. After stirring at room temperature for 2 h, the final solution was prepared by adjusting to pH 8.5 with NaOH aqueous solution (1 M) and then adding 1.3 mg ABC. After 24 h stirring, the $Bi_2S_3$@Bi@PDA NRs were obtained by centrifuging at 10,000 rpm for 5 min and washing with D.I. water at least 3 times.

### 2.4. *Preparation of $Bi_2S_3$@Bi@PDA-HA NRs*

Briefly, $Bi_2S_3$@Bi@PDA NRs (2 mg/ml, 10 ml) was mixed with HA (10 mg/ml, 10 ml) in D.I. water stirred moderately for 12 h. Through centrifugation and washing by D.I. water twice, the HA-modified $Bi_2S_3$@Bi@PDA NRs ($Bi_2S_3$@Bi@PDA-HA NRs) were collected.

### 2.5. *Drug loading and release profile measurement*

10 mg $Bi_2S_3$@Bi NRs was sonicated and dispersed into 100 ml of 10 mM tris solution containing 1 mg DA·HCl and 5 mg Art. After stirring for 2 h, the final solution was adjusted to pH 8.5 with NaOH aqueous solution (1 M), and then added 1.3 mg ABC. After stirring at 25 °C for a further 24 h, the $Bi_2S_3$@Bi@PDA-Art NRs were obtained by centrifuging at 10,000 rpm for 5 min and washing with D.I. water

at least 3 times. The clear supernatant was extracted by centrifugation and the content of Art was analyzed by high-performance liquid chromatography (HPLC) (Agilent 1200). 10 μl the supernatant was eluted with a mobile phase consisting of acetonitrile-water (60:40, v/v). And the detection wavelength was 235 nm.

The drug release profile of Art from $Bi_2S_3$@Bi@PDA-Art NRs was carried out in PBS release medium at different pH values (pH 4.0 and 7.0) and NIR-triggered drug release was analyzed under laser irradiation (808 nm, 1.0 W/cm$^2$, 6 min). Briefly, the $Bi_2S_3$@Bi@PDA-Art NRs were dispersed into centrifugal tubes containing PBS buffer solution (pH 7.0 or 4.0) under stirring at 200 rpm. At the given time points, 200 μl each sample was centrifuged at 10,000 rpm for 5 min to get supernatant. After that, concentrations of released Art in the medium were analyzed by HPLC.

### 2.6. Fluorescence imaging

The 4T1 cells were cultured in 24-well plates at $2 \times 10^4$ cells per well. After overnight incubation, the original medium was removed and another 200 μl medium containing $Bi_2S_3$@Bi@PDA-HA/FITC NRs (50 μg/ml) was added. After incubation for 6 h, the medium was aspirated and the coverslips were rinsed with PBS 3 times and fixed with 4% paraformaldehyde at room temperature for 30 min. For the staining experiment, DAPI (1 μg/ml) and Lyso-Tracker Red (50 nM) were dropped into culture medium and co-stained for another 30 min. Finally, the coverslips were washed with PBS 3 times and then mounted on microscope slides for visualization using a confocal microscopy study (CLSM, Leica TCS SP5) and the fluorescent images were analyzed by Image J software.

### 2.7. Cytotoxicity assay

A standard MTT assay was performed to characterize the cell cytotoxicity of $Bi_2S_3$@Bi@PDA-HA NRs to LO2 cells. Typically, the LO2 cells were cultured in 96-well plates at $8 \times 10^3$ cells per well. After overnight incubation, the $Bi_2S_3$@Bi@PDA-HA NRs were added to the RPMI 1640 medium with concentrations of 0, 10, 50, 100, 150 and 200 μg/ml. Then, the MTT assay was performed, and the results were detected by a microplate reader.

The synergistic effects of $Bi_2S_3$@Bi@PDA-HA NRs against cancer cells were also measured by standard MTT assay. 4T1 cells were cultured in 96-well plates at $5 \times 10^3$ cells per well for 12 h. Different concentrations of $Bi_2S_3$@Bi@PDA-HA NRs and $Bi_2S_3$@Bi@PDA-HA/Art NRs were added to the cell culture medium and incubated with the cells for 6 h under normoxic conditions (21% $O_2$, 5% $CO_2$). Then the cells were irradiated with a NIR laser (808 nm, 1.0 W/cm$^2$, 6 min). After incubating at 37 °C for another 18 h, the MTT assay was performed and the results were detected by microplate reader. The same experiment was repeated under hypoxic conditions (2% $O_2$, 5% $CO_2$).

### 2.8. In vivo antitumor efficiency of $Bi_2S_3$@Bi@PDA-HA NRs

The 4T1 tumor-bearing BALB/c mice were used as the tumor model by injecting a total number of $1.0 \times 10^6$ 4T1 cells subcutaneously into the right dorsal region of BALB/c mice. When the tumors reached ~100 mm$^3$, the mice were randomly distributed into seven groups ($n = 6$): (1) PBS, (2) PBS+NIR, (3) $Bi_2S_3$@Bi@PDA-HA NRs, (4) Art, (5) $Bi_2S_3$@Bi@PDA-HA/Art NRs, (6) $Bi_2S_3$@Bi@PDA-HA NRs + NIR, (7) $Bi_2S_3$@Bi@PDA-HA/Art NRs + NIR. The prepared formulations were injected intravenously into mice at the dose of $Bi_2S_3$@Bi@PDA-HA NRs (5 mg/kg), $Bi_2S_3$@Bi@PDA-HA/Art NRs (5 mg/kg), Art (0.5 mg/kg), and PBS (100 μl) on Day 0. At 8 h after intravenous injection, for groups (2, 6 and 7), a laser (808 nm, 1.0 W/cm$^2$, 6 min) was applied to the mice. The tumor size and body weight were measured every day for 14, and the tumor volume was calculated as V = (tumor length × tumor width$^2$)/2. On Day 14 after therapy, animals were sacrificed and their tumors were harvested for the photograph and hematoxylin-eosin (H&E) staining. The tumor growth inhibition rate (TGI%) was calculated using the following equation:

$$TGI\% = \frac{V_c - V_t}{V_c - V_0} \times 100$$

where $V_c$ and $V_t$ are the tumor volumes of control and after treatment on Day 14 and $V_0$ is the mean tumor volume on Day 0.

### 2.9. In vivo thermal imaging of tumors

The tumor-bearing mice were intravenously injected with 100 μl PBS containing 100 μg $Bi_2S_3$@Bi@PDA-HA NRs. The tumor region was treated with 808 nm laser (1.0 W/cm$^2$, 6 min) at predetermined time intervals ($t = 0$, 2, 4, 8, 12 and 24 h), and the temperature at the tumor region was detected by thermal imaging (FLIR).

For *in vivo* thermal imaging, the $Bi_2S_3$@Bi@PDA-HA NRs were dispersed in PBS (100 μl) and intravenously injected into the tumor-bearing mice. After 8 h injection, the entire tumor region of animals was treated with 808 nm NIR laser at a power intensity of 1.0 W/cm$^2$ for 6 min. During the laser irradiation, a thermal imager was used to observe full-body infrared (IR) thermal images.

### 2.10. Statistical analysis

The mean value ± standard deviation (SD) was presented for all measurement data. One-way analysis of variance (ANOVA) was performed for statistical analysis. The difference between the two groups was considered to be significant for $^*P < 0.05$ and $^{***}P < 0.001$, respectively.

## 3. Results and discussion

### 3.1. Synthesis and characterization of $Bi_2S_3$@Bi@PDA-HA NRs

The orthorhombic $Bi_2S_3$ samples were synthesized via a facile solvothermal method [18]. Transmission electron microscopy (TEM) image (Fig. S1A) showed that the $Bi_2S_3$ particles were ~120 nm in length and ~30 nm in width with nanorod-like morphology. Bi-layer was further grown on $Bi_2S_3$ NRs through hydrazine treatment of $Bi_2S_3$ NRs to form $Bi_2S_3$@Bi NRs. TEM

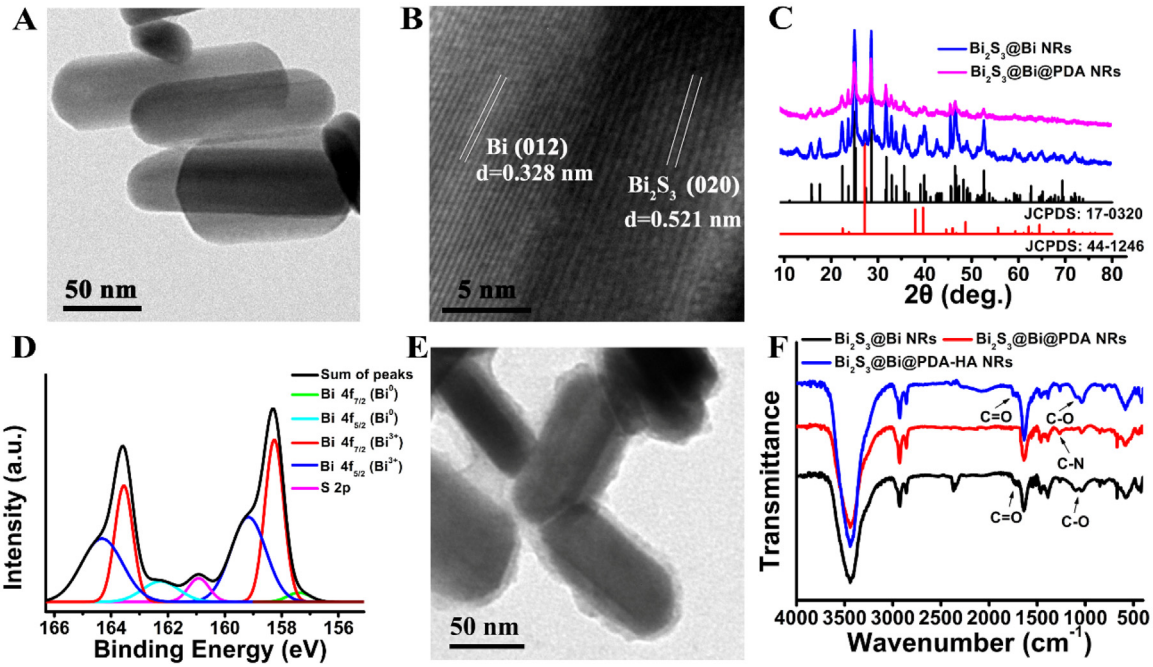


**Fig. 1 – Characterization of $Bi_2S_3$@Bi NRs-based nanomaterials. (A) TEM image of $Bi_2S_3$@Bi NRs. (B) HRTEM lattice fringes of $Bi_2S_3$@Bi NRs. (C) XRD patterns of $Bi_2S_3$@Bi NRs and $Bi_2S_3$@Bi@PDA NRs. (D) Bi 4f XPS spectra of $Bi_2S_3$@Bi NRs. (E) TEM image of $Bi_2S_3$@Bi@PDA NRs. (F) FTIR spectra of $Bi_2S_3$@Bi NRs-based nanomaterials.**

images (Fig. 1A) revealed that the synthesized $Bi_2S_3$@Bi NRs had a thin Bi layer on the surface with an aspect ratio of ~3.5 (length: ~140 nm, width: ~40 nm). The lattice fringes of $Bi_2S_3$@Bi NRs corresponded to the (020) and (012) planes of $Bi_2S_3$ and Bi were well-resolved in the high-resolution TEM (HRTEM) image with interplanar spacings of 0.521 nm and 0.328 nm, respectively (Fig. 1B) [26,27]. In contrast, without $Bi_2S_3$ NRs, pure Bi was composed of spherical particles (Fig. S1B). The X-ray diffraction (XRD) patterns of $Bi_2S_3$@Bi NRs (Fig. 1C) exhibited diffraction peaks indexed to the orthorhombic $Bi_2S_3$ phase (JCPDS no. 17-0320) [28] and rhombohedral Bi-layers (JCPDS no. 44-1246) [29], respectively. Moreover, X-ray photoelectron spectroscopy (XPS) was used to analyze the chemical composites of $Bi_2S_3$@Bi NRs. The Bi $4f_{7/2}$ and Bi $4f_{5/2}$ XPS spectra peaks of $Bi_2S_3$@Bi NRs were 163.6 eV/158.3 eV and 164.6 eV/159.3 eV respectively, indicating the presence of $Bi^{3+}$ in $Bi_2S_3$ NRs (Fig. 1D) [30], while the peaks at 162.3 eV and 157.2 eV were attributed to $Bi^0$ in Bi-layers [31]. These results indicated the successful synthesis of the heterostructured $Bi_2S_3$@Bi NRs. UV–vis-NIR spectrum (Fig. S2A) suggested that $Bi_2S_3$@Bi NRs had wide absorption in the NIR region, implying that they could be used as photothermal agents.

PDA/ammonium bicarbonate ($NH_4HCO_3$, ABC) was coated on the surface of $Bi_2S_3$@Bi NRs via the self-polymerization of dopamine in a mild basic environment (pH 8.5) [24]. The morphology of $Bi_2S_3$@Bi NRs was analyzed by TEM. As shown in Fig. 1E, PDA/ABC coating did not change the shape but formed a smooth layer on the surface of $Bi_2S_3$@Bi NRs. The PDA layer had an average thickness of 7 nm. Furthermore, the addition of PDA/ABC increased the hydrodynamic size of the NRs from 154.57 ± 3.62 nm to 204.87 ± 3.14 nm (Fig. S2B) and changed the zeta potential from −8.47 ± 0.55 mV to −13.63 ± 0.83 mV (Fig. S2C). The XRD data depicted that the structure of $Bi_2S_3$@Bi NRs was not altered during the modification process (Fig. 1C). In Fourier translation infrared (FTIR) spectra, the characteristic bands of the C=O and C–O stretching in the ester group of Tween-20 at 1720 $cm^{-1}$ and 1050 $cm^{-1}$ disappeared (Fig. 1F). Meanwhile, the spectra showed the existence of the absorbance band at 1260 $cm^{-1}$, which was assigned to the C–N stretching in the PDA shell. All the data strongly supported the successful modification of the PDA. Subsequently, the tumor-targeting ability of the nanoplatform was achieved by HA modification via the hydrogen bond and electrostatic interactions between HA and PDA [32]. The TEM imaging (Fig. S3A) showed that HA modification did not affect the morphology of $Bi_2S_3$@Bi@PDA NRs. Besides, the hydrodynamic size and zeta potential of the NRs shifted to 254.15 ± 4.57 nm and −32.37 ± 1.16 mV, respectively (Fig. S2B and C). Furthermore, the FTIR spectra (Fig. 1F) displayed the reappearance of characteristic bands at 1720 $cm^{-1}$ and 1050 $cm^{-1}$ due to the C=O and C–O stretching in the ester group of HA. These results confirmed that HA was wrapped around the $Bi_2S_3$@Bi@PDA NRs.

### 3.2. *In vitro $O_2$ evolution, ROS production, and photothermal behavior*

The electron–hole separation ability guided by the Z-scheme mechanism made $Bi_2S_3$@Bi NRs capable of producing $O_2$ and ROS under NIR irradiation. Substantial $O_2$ production in the $Bi_2S_3$@Bi NRs suspension upon 808 nm laser irradiation was monitored by the dissolved $O_2$ meter. Meanwhile, the DCFH probe was selected to investigate the ROS generation ability of $Bi_2S_3$@Bi NRs. As shown in Fig. S4A and S4B, under NIR irradiation, $Bi_2S_3$@Bi NRs could produce $O_2$ and ROS in a

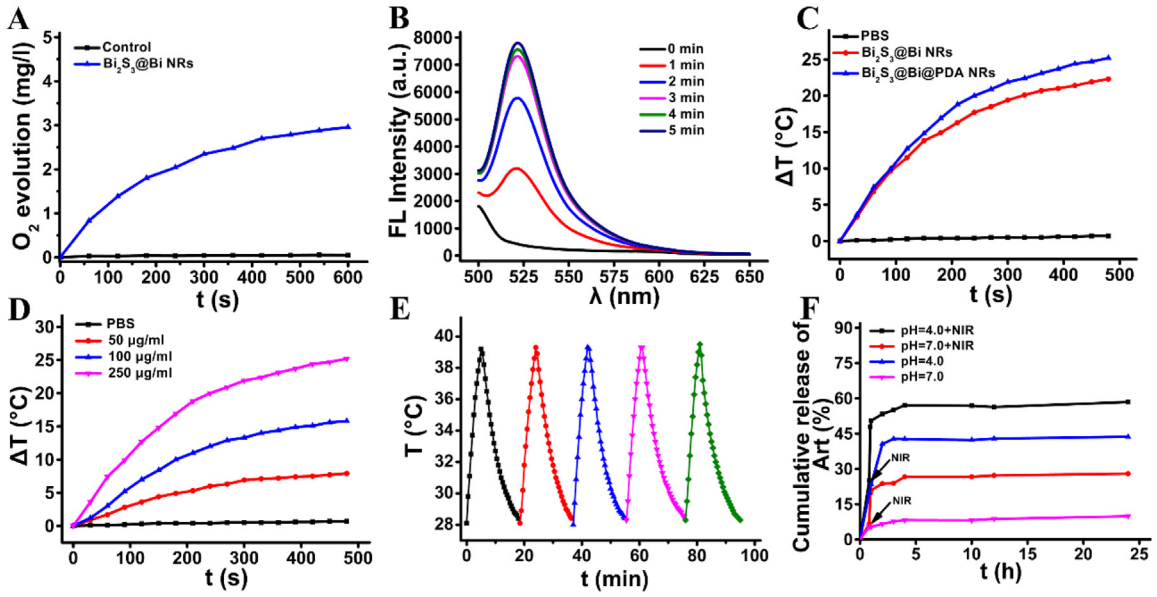


**Fig. 2 – (A) $O_2$ generation curves of $Bi_2S_3$@Bi NRs under laser irradiation (808 nm, 1.0 W/cm$^2$, 10 min). (B) The fluorescence increment of DCF at 525 nm in $Bi_2S_3$@Bi NRs aqueous suspension upon laser irradiation (808 nm, 1.0 W/cm$^2$, 5 min). (C) Photothermal response of $Bi_2S_3$@Bi NRs and $Bi_2S_3$@Bi@PDA NRs upon laser irradiation (808 nm, 1.0 W/cm$^2$, 8 min). (D) Photothermal heating curves of $Bi_2S_3$@Bi@PDA NRs aqueous suspension with varied concentrations (PBS, 50, 100, and 250 μg/ml) using an 808 nm laser (1.0 W/cm$^2$). (E) Photothermal stability curves of $Bi_2S_3$@Bi@PDA NRs for five laser on/off cycles under irradiation (808 nm, 1.0 W/cm$^2$). (F) The Art release profiles of $Bi_2S_3$@Bi@PDA-Art NRs at pH 4.0 and 7.0 with or without 808 nm laser irradiation (1.0 W/cm$^2$, 6 min).**

radiant energy-dependent manner. Since high laser power could cause photodamage to normal tissues [33,34], the laser power used in the subsequent experiments was chosen as 1.0 W/cm$^2$. At the selected power, $Bi_2S_3$@Bi NRs with a concentration of 100 μg/ml under 808 nm laser irradiation (1.0 W/cm$^2$, 6 min) produced 2.96 mg/l of $O_2$ in 10 min (Fig. 2A). And a time-dependent increase in the fluorescence intensity of DCF was observed in the solution of $Bi_2S_3$@Bi NRs (Fig. 2B). Besides, the $O_2$ and ROS generation ability of $Bi_2S_3$@Bi NRs could not be affected by the presence of $H_2O_2$ (Fig. S4C and S4D). All these results demonstrated that $Bi_2S_3$@Bi NRs could achieve $O_2$ self-supply and ROS production in an $H_2O_2$-independent and spatiotemporally synchronous manner for hypoxic tumor therapy.

Subsequently, the photothermal behavior of $Bi_2S_3$@Bi@PDA NRs was examined under NIR irradiation by assessing their temperature elevation profile. The temperatures of $Bi_2S_3$@Bi@PDA NRs and $Bi_2S_3$@Bi NRs suspensions (250 μg/ml) were increased by 25.2 and 22.3 °C (Fig. 2C), respectively, after irradiation by 808 nm laser for 8 min at the power density of 1.0 W/cm$^2$. In contrast, PBS showed negligible temperature variation upon irradiation, indicating the outstanding photothermal property of $Bi_2S_3$@Bi@PDA NRs. The photothermal conversion efficiency ($\eta$) of $Bi_2S_3$@Bi@PDA NRs was calculated to be 23.35% (Fig. S5), higher than that of $Bi_2S_3$@Bi NRs ($\eta$ = 21.74%, Fig. S5), which was probably due to the strong NIR absorption and high photothermal conversion efficiency of PDA ($\eta$ = 27.32%, Fig. S5) [35]. We further monitored the dose-dependent heat generation capability of $Bi_2S_3$@Bi@PDA NRs, and a concentration-dependent temperature elevation was observed from 50 to 250 μg/ml (Fig. 2D). The photothermal effect of $Bi_2S_3$@Bi@PDA NRs also exhibited a radiant energy-dependent fashion (Fig. S6A). Moreover, $Bi_2S_3$@Bi@PDA NRs showed a limited change in heating impact, even after five cycles of heating and cooling, indicating $Bi_2S_3$@Bi@PDA NRs exhibited good photothermal stability (Fig. 2E). These results confirmed the excellent photothermal performance of $Bi_2S_3$@Bi@PDA NRs.

### 3.3. *Drug loading behavior, in vitro drug release kinetics, and stability*

Subsequently, the potential of $Bi_2S_3$@Bi@PDA-HA NRs as drug carriers to encapsulate Art was examined. The Art loading capability of $Bi_2S_3$@Bi@PDA-HA NRs was quantitated by HPLC, which was calculated to be 100.23 μg (Art)/mg ($Bi_2S_3$@Bi@PDA-HA/Art NRs), providing a strong guarantee for the following anti-tumor studies. Besides, Art loading did not affect the morphology, hydrodynamic size, and zeta potential of $Bi_2S_3$@Bi@PDA-HA NRs (Figs. S2B, S2C and S3B). Most importantly, excellent photothermal performance as well as ROS and $O_2$ production efficiency of $Bi_2S_3$@Bi@PDA-HA/Art NRs were also observed (Fig. S6B–S6F).

The microenvironment of solid tumors is known to be more acidic than the physiological condition of normal tissue, which can be attributed to the tumors' increased glycolytic flux [36,37]. Under acidic conditions, ABC in the PDA shell could be decomposed into $CO_2$ and $NH_3$, resulting in a "bomb-like" release of Art [24]. The drug release profile of $Bi_2S_3$@Bi@PDA-Art NRs was monitored in PBS at different pH

values and the NIR-triggered drug release was analyzed under laser irradiation. The drug release profile showed Art from $Bi_2S_3$@Bi@PDA-Art NRs released extremely fast under acidic conditions (pH 4.0) that imitated the lysosomal environment in cancer cells, while only 9.90% of the drug was released in 24 h under physiological conditions (pH 7.0) (Fig. 2F), indicating the protection and drug-preserving ability of the PDA shell. More importantly, both at pH 7.0 and pH 4.0, the release of Art was significantly increased under 808 nm laser irradiation (1.0 W/cm$^2$, 6 min) (Fig. 2F and S7), owing to the decomposition of ABC under the local heat generated by the $Bi_2S_3$@Bi@PDA NRs and then the destruction of the PDA layer. More importantly, as demonstrated by the results of UV–vis-NIR spectroscopy, HPLC, and mass spectrometry, the photothermal effect could not destroy the structure of Art (Fig. S8). These data suggested that $Bi_2S_3$@Bi@PDA NRs as the TME/NIR-responsive drug delivery nanosystem allowed for controlled drug release as well as reduced the side effect of the chemotherapeutic agents.

The stability of the nanoplatform is an important parameter for future clinical applications. Therefore, the morphology and hydrodynamic size of $Bi_2S_3$@Bi@PDA-HA/Art NRs in different solutions (D.I. water, PBS buffer (pH 7.4), and cell culture medium (RPMI 1640 supplemented with 10% fetal bovine serum)) were investigated. DLS and TEM results in Fig. S9 showed that the particle size and morphology of $Bi_2S_3$@Bi@PDA-HA/Art NRs changed little after standing for 14 d, revealing the good stability of $Bi_2S_3$@Bi@PDA-HA/Art NRs, which suggested their potential for antitumor application.

### 3.4. *Endocytosis and intracellular hypoxia level/ROS detection*

The HA coating on the surface of the $Bi_2S_3$@Bi@PDA-HA NRs could significantly increase their accumulation in targeted cancer cells. FITC was loaded into $Bi_2S_3$@Bi@PDA-HA NRs to act as the fluoresce probe to investigate the cellular uptake of $Bi_2S_3$@Bi@PDA-HA NRs in 4T1 cells, followed by DAPI and Lyso-Tracker Red staining after 6 h of incubation. The emission signal of $Bi_2S_3$@Bi@PDA-HA/FITC NRs overlapped well with Lyso-Tracker Red in 4T1 cells (Fig. 3A). In contrast, the minimal fluorescent signal of $Bi_2S_3$@Bi@PDA-HA/FITC NRs was observed in CD44-negative LO2 cells (Fig. S10A). And the fluorescence intensity in 4T1 cells treated with $Bi_2S_3$@Bi@PDA-HA/FITC NRs was ~3.35 folds higher than that in LO2 cells (Fig. S10B). Our results showed that the HA layer enabled the nanoplatform to get endocytosed by CD44-positive cells. The highly acidic environment in lysosome facilitated the release of Art, promoting ferritin degradation and thus inducing the pool of free iron in cancer cells, leading to notable ferroptosis [38,39]. This receptor-mediated internalization of nanoplatform would greatly improve its therapeutic outcome in specific cancers.

Sufficient $O_2$ supply is essential for increasing ROS yield in order to improve PDT efficacy. The intracellular $O_2$-evolving performance of $Bi_2S_3$@Bi@PDA-HA NRs was estimated using a fluorescence quenching assay with RDPP, an indicator for $O_2$ [40]. In 4T1 cells, the fluorescence of RDPP was quenched under normoxic conditions (21% $O_2$) (Fig. S11), whereas under hypoxic conditions (Fig. 3B, group 1), strong red fluorescence

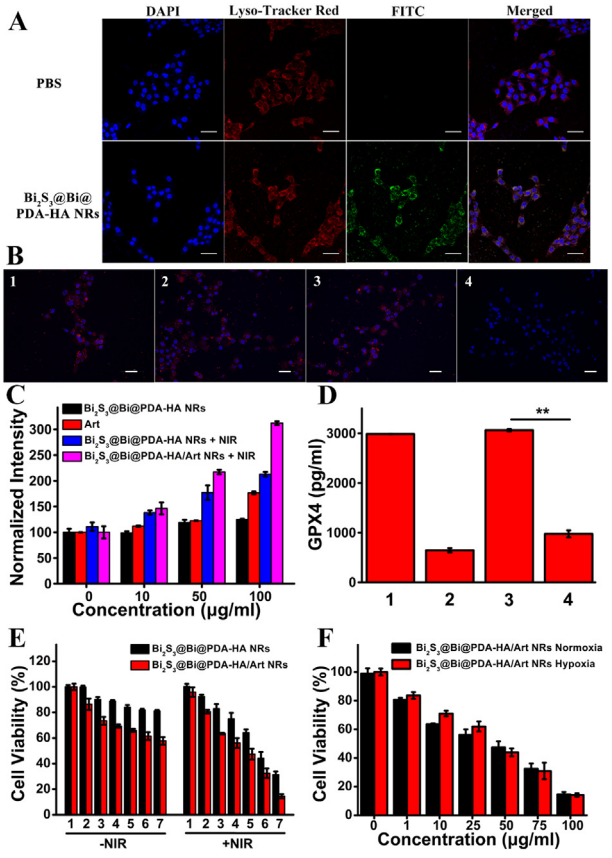


**Fig. 3 – (A) CLSM images showing co-localization of $Bi_2S_3$@Bi@PDA-HA NRs with lysosomes in 4T1 cells. Scale bar = 50 μm. (B) Cellular $O_2$ level of 4T1 cells stained by RDPP in hypoxia condition. Scale bars = 50 μm. (C) Fluorescence detection of ROS after being treated with NRs with and without 808 nm laser irradiation (1.0 W/cm$^2$). (D) ELISA analysis of GPX4 in 4T1 cells treated by (1) PBS, (2) Art, (3) $Bi_2S_3$@Bi@PDA-HA NRs + NIR and (4) $Bi_2S_3$@Bi@PDA-HA/Art NRs + NIR. (E) Cell viability after incubating with various concentrations of different NRs with or without laser irradiation (808 nm, 1.0 W/cm$^2$, 6 min) in normoxia condition (note that:1–7 respectively represent the concentration of NRs 0, 1, 10, 25, 50, 75, 100 μg/ml). (F) Cell viability after incubating with various concentrations of $Bi_2S_3$@Bi@PDA-HA/Art NRs with laser irradiation (808 nm, 1.0 W/cm$^2$, 6 min) in normoxia condition and hypoxia condition.**

was observed. The laser irradiation (Fig. 3B, group 2) and $Bi_2S_3$@Bi@PDA-HA NRs (Fig. 3B, group 3) themselves could not increase the $O_2$ level in 4T1 cells. However, in comparison with the untreated group, laser irradiation substantially weakened the fluorescence signals in $Bi_2S_3$@Bi@PDA-HA NRs treated 4T1 cells (Fig. 3B, group 4), indicating the excellent $O_2$ supplying ability of $Bi_2S_3$@Bi@PDA-HA NRs upon NIR irradiation for relieving the hypoxia. Moreover, the results of fluorescence images (Fig. S12A) and fluorescence quantitative analysis (Fig. S12B) proved that the $O_2$ production ability of $Bi_2S_3$@Bi@PDA-HA NRs was barely influenced by the introduction of Art.

The endoperoxide bridge in Art has been shown to react with endogenous $Fe^{2+}$ ions to produce efficient free radicals $O_2^-$ for ROS amplification [41]. The intracellular $Fe^{2+}$ ions measured in human normal liver LO2 cells and cancer cells (4T1 cells) revealed that $Fe^{2+}$ ions in 4T1 cells had 2.3-fold higher than that in LO2 cells (Fig. S13), which endowed Art with the ability to initiate tumor-specific chemotherapeutic effects. DCFH-DA which could be oxidized to green fluorescent 2′,7′-dichlorofuorescin (DCF) by ROS was utilized to detect the intracellular ROS generation induced by different treatments [42]. As shown in Fig. S14, an increase in fluorescence signal was observed in Art-treated 4T1 cells compared to that in LO2 cells. The ROS fluorescence images in Fig. S15 and their corresponding quantitative analysis by Image J software in Fig. S16 showed that $Bi_2S_3$@Bi@PDA-HA NRs themselves induced a negligible change in DCF fluorescence in 4T1 cells. However, the fluorescence signals in $Bi_2S_3$@Bi@PDA-HA NRs treated cells were significantly increased by 808 nm laser irradiation, suggesting the photodynamic performance of $Bi_2S_3$@Bi@PDA-HA NRs. Moreover, owing to the therapeutic effects of Art, the addition of Art increased the intracellular ROS level, especially in PDT-treated 4T1 cells. In addition, the intracellular ROS level was also measured quantitatively by the same probe using a fluorescence spectrophotometer. As indicated in Fig. 3C, $Bi_2S_3$@Bi@PDA-HA/Art NRs with laser irradiation induced significantly higher ROS levels compared with other groups. Especially, the extent of generated ROS induced by $Bi_2S_3$@Bi@PDA-HA/Art NRs (100 μg/ml) was ~1.47-fold greater than that induced by $Bi_2S_3$@Bi@PDA-HA NRs (100 μg/ml) after laser irradiation (Fig. 3C), indicating that $Bi_2S_3$@Bi@PDA-HA/Art NRs exhibited the strongest ROS generation efficiency under laser irradiation due to the synergistic effect of $Bi_2S_3$@Bi NRs mediated PDT and Art-induced CDT.

PDT has been shown to increase the expression of GPX4 and cellular concentration of GSH in cancer cells, both of which can degrade the generated ROS, resulting in PDT resistance [43,44]. However, Art can induce ferroptosis by consuming intracellular GSH and decreasing the GPX4 levels [23]. As a result, combining Art-mediated CDT with PDT would significantly increase the intracellular ROS levels and sensitize cancer cells to PDT, potentially improving the therapeutic outcomes. To support our hypothesis, we monitored the GPX4 activity and GSH/GSSG ratio following different treatments. The GPX4 level in $Bi_2S_3$@Bi@PDA-HA NRs treated cells increased slightly after 808 nm laser irradiation (Fig. 3D). However, the GPX4 level in $Bi_2S_3$@Bi@PDA-HA NRs administered group decreased from 3063.85 pg/ml to 974.22 pg/ml after laser irradiation due to the inhibition effect of Art on GPX4 expression (Fig. 3D). Furthermore, the significantly lower GSH/GSSG ratio in $Bi_2S_3$@Bi@PDA-HA/Art NRs pretreated cells after PDT treatment also indicated the increased oxidative stress (Fig. S17), which resulted in an enhanced anti-cancer effect.

### 3.5. *In vitro anti-cancer effect*

Next, we assessed the synergistic therapeutic efficiency of $Bi_2S_3$@Bi@PDA-HA/Art NRs *in vitro* due to their superior photothermal impact, ROS production capacity, and TME-responsive drug release behavior. MTT assay was used to assess the cytotoxicity of free Art and $Bi_2S_3$@Bi@PDA-HA/Art NRs on 4T1 cells. $Bi_2S_3$@Bi@PDA-HA/Art NRs exhibited a dose-dependent cytotoxic activity comparable to free Art (Fig. S18A). However, the $Bi_2S_3$@Bi@PDA-HA NRs showed negligible cytotoxicity to 4T1 cells even at a high concentration of up to 100 μg/ml (Fig. 3E), indicating that the cytotoxicity of $Bi_2S_3$@Bi@PDA-HA/Art NRs was due to Art. Moreover, laser irradiation had shown the potential to substantially improve the anti-cancer efficacy of both $Bi_2S_3$@Bi@PDA-HA NRs and $Bi_2S_3$@Bi@PDA-HA/Art NRs by increasing the cytotoxicity of the nanoplatform. For example, the viability of 4T1 cells decreased to 31.41% and 14.53%, respectively, after $Bi_2S_3$@Bi@PDA-HA NRs (100 μg/ml) and $Bi_2S_3$@Bi@PDA-HA/Art NRs (100 μg/ml) treatments. These results demonstrated that combinatorial phototherapy with Art-induced CDT resulted in more severe cell injuries. Besides, the *in vitro* cytotoxicity of $Bi_2S_3$@Bi@PDA-HA/Art NRs in 4T1 cells was also studied in hypoxic (2% $O_2$) conditions due to the ability of $Bi_2S_3$@Bi@PDA-HA NRs to generate $O_2$. The cell viabilities of both the $Bi_2S_3$@Bi@PDA-HA NRs and $Bi_2S_3$@Bi@PDA-HA/Art NRs treated cells after 808 nm laser irradiation (1.0 W/cm$^2$, 6 min) were comparable to that obtained under normoxic conditions (Figs. 3E, 3F and S18B), validating that $Bi_2S_3$@Bi@PDA-HA NRs could still induce potent cell injury in hypoxia condition. Meanwhile, the *in vitro* therapeutic effect of nanoplatform on 4T1 cells was also recorded by live/dead cell staining assay. Under normoxic conditions (Fig. S19A), NIR irradiation and single $Bi_2S_3$@Bi@PDA-HA NRs showed little damage to 4T1 cells (most of them exhibited green fluorescence). A small part of 4T1 cells received Art or $Bi_2S_3$@Bi@PDA-HA/Art NRs were killed, which clearly showed the therapeutic effect of Art *in vitro*. However, $Bi_2S_3$@Bi@PDA-HA NRs under the NIR irradiation induced a large amount of cell death as revealed by the conspicuous red fluorescence in 4T1 cells. In particular, the vast majority of dead cells were observed in the $Bi_2S_3$@Bi@PDA-HA/Art NRs + NIR irradiation group, which showed almost all red PI fluorescence in the view. The *in vitro* Calcein-AM/PI staining experiments were also studied in hypoxic (2% $O_2$) conditions. And the results in hypoxic conditions were comparable to that obtained under normoxic conditions (Fig. S19B). Notably, the cell staining results from Fig. S19 were consistent with the MTT assays and highlighted the synergistic effect of PDT and PTT as well as Art-induced CDT in cancer treatment.

### 3.6. *In vitro and in vivo biocompatibility study*

The biocompatibility of the nanoplatform should be thoroughly assessed in order to further demonstrate its suitability for cancer treatment. MTT assay showed that more than 85% of $Bi_2S_3$@Bi@PDA-HA NRs treated LO2 cells remained alive after 24 h treatment, even at a concentration of 200 μg/ml (Fig. S20A). Moreover, the hemolysis assay showed only 1% hemolysis after $Bi_2S_3$@Bi@PDA-HA NRs treatment within the range of 1-100 μg/ml, which was below the clinically acceptable limit (Fig. 4A) [45]. Furthermore, biocompatibility studies were carried out in order to investigate the safety of $Bi_2S_3$@Bi@PDA-HA NRs. As shown in Fig. 4B, there was a negligible difference in body weight fluctuations between the $Bi_2S_3$@Bi@PDA-HA NRs-treated mice and PBS-treated

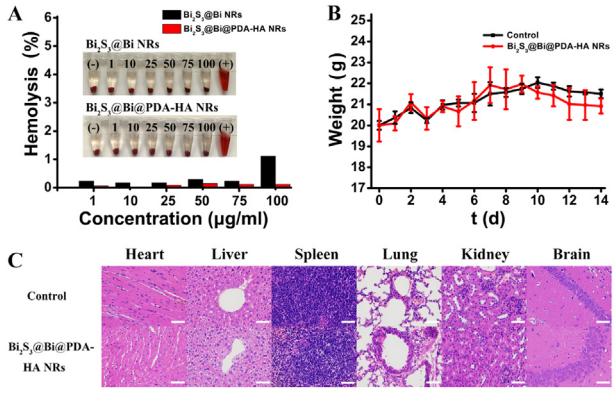


**Fig. 4 – (A) Hemolysis assays for $Bi_2S_3$@Bi NRs and $Bi_2S_3$@Bi@PDA-HA NRs. The concentration of NRs varied from 1 μg/ml to 100 μg/ml. (mean ± SD, *n* = 3 for each sample). (B) The relative body weights with different treatments from tumor-free mice. (mean ± SD, *n* = 6 for each sample). (C) H&E-stained images of main organ slices were collected from tumor-free mice of the different groups. Scale bar = 50 μm.**

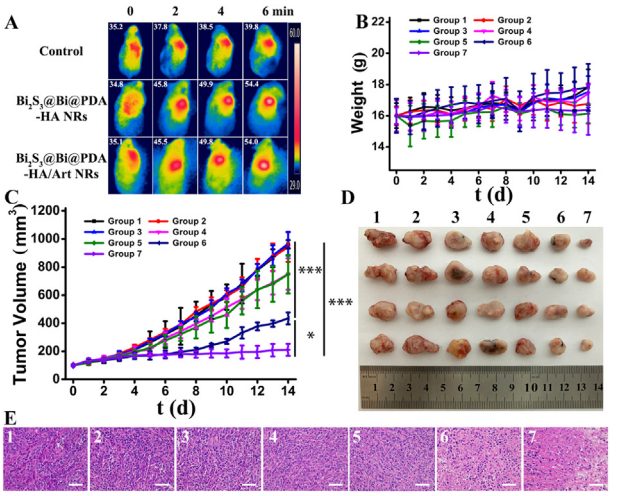


**Fig. 5 – (A) The IR thermal imaging of tumor-bearing mice intravenously injected with PBS, $Bi_2S_3$@Bi@PDA-HA NRs or $Bi_2S_3$@Bi@PDA-HA/Art NRs at 8 h exposing to 808 nm laser irradiation (1.0 W/cm², 6 min). (B) The body weights of different groups after various treatments. Mean ± SD, *n* = 6 for each group. (C) Tumor growth curves of mice after intravenous injection with PBS, Art, $Bi_2S_3$@Bi@PDA-HA NRs, and $Bi_2S_3$@Bi@PDA-HA/Art NRs with or without NIR laser irradiation within 14 days (*n* = 6, ***P < 0.001, *P < 0.05). (D) The photographs and (E) H&E stained images of tumors from different groups. Scale bar = 50 μm. Note that: (1)PBS, (2)PBS + NIR, (3)$Bi_2S_3$@Bi@PDA-HA NRs, (4)Art, (5)$Bi_2S_3$@Bi@PDA-HA/Art NRs, (6)$Bi_2S_3$@Bi@PDA-HA NRs + NIR, (7)$Bi_2S_3$@Bi@PDA-HA/Art NRs + NIR.**

mice within 14 d (Fig. 4B). Besides, the parameters of blood routine and blood biochemical tests were conducted at 14 d after administration of the NRs. Kidney and liver function indicators, as well as the hematology markers, maintained normal compared with the control group (Fig. S20B–S20D and Table S1). Besides, H&E staining was also performed to evaluate the tissue harvested at 14 d to observe the pathological changes. The results of the main organs (hearts, livers, spleens, lungs, kidneys, and brains) in the two groups were similar with no abnormalities (Fig. 4C). These findings indicated that the synthesized $Bi_2S_3$@Bi@PDA-HA NRs were biocompatible and safe for *in vivo* therapeutic applications.

### 3.7. *In vivo antitumor effects*

It has been reported that photo-irradiation with relatively high laser power can cause photodamage to normal tissues [46,47]. In order to avoid photodamage caused by laser irradiation alone in the *in vivo* experiments, the optimal power density of the 808 nm laser was examined in PBS-treated mice. According to the previous literatures, higher temperature exceeding a certain threshold (43 °C) can cause cell lesion damage [47]. As shown in Fig. S21, by increasing the laser power from 1.0 to 1.1 W/cm², the temperature in tumor sites gradually elevated to 43.4 °C during the 6 min of laser irradiation, which confirmed laser power density played a critical role in preventing normal tissue injury. Considering that lower power density was not conducive to achieving the satisfactory therapeutic effect of $Bi_2S_3$@Bi@PDA-HA NRs at low doses, 1.0 W/cm² was chosen as the optimal laser power density in the following *in vivo* experiments.

To assess the *in vivo* synergistic effects of PDT/PTT/CDT, 4T1-tumor-bearing BALB/c mice were used. The *in vivo* cancer-targeting capacity of $Bi_2S_3$@Bi@PDA-HA NRs was first evaluated using thermal imagines, which was critical for their antitumor effect. The signals of tumor areas gradually strengthened up to 8 h after injection, as displayed by the IR thermal images (Fig. S22). Moreover, 8 h after intravenous injection, the accumulation of $Bi_2S_3$@Bi@PDA-HA NRs in tumor tissues of 4T1-tumor-bearing BALB/c mice (11.77% ± 2.58% ID/g) was also observed by an inductively coupled plasma-atomic emission spectrometer (ICP-AES) (Fig. S23). These results supported the passive accumulation of $Bi_2S_3$@Bi@PDA-HA NRs in tumor areas.

Furthermore, *in vivo* thermal images displayed that a rapid increase in temperature to 54.4 °C was observed in the tumor area of the mice treated with $Bi_2S_3$@Bi@PDA-HA NRs within 6 min by laser irradiation while the temperature only changed from 35.2 °C to 39.8 °C in PBS-treated mice (Fig. 5A), suggesting the excellent photothermal effect of $Bi_2S_3$@Bi@PDA-HA NRs *in vivo*. Overall, our results showed that the developed $Bi_2S_3$@Bi@PDA-HA NRs could be accumulated in the tumor region and exert a strong anti-cancer effect.

To further investigate the potency of the multifunctional nanoplatform to alleviate hypoxia *in vivo*, a hypoxia-sensing probe (pimonidazole hydrochloride) was employed to observe the tumor hypoxic areas. As shown in Fig. S24, compared with the control group, a significantly reduced green immunofluorescence signal in tumor slices was observed in the groups of $Bi_2S_3$@Bi@PDA-HA NRs + NIR and $Bi_2S_3$@Bi@PDA-HA/Art NRs + NIR, showing that $Bi_2S_3$@Bi@PDA-HA/Art NRs under NIR irradiation had excellent hypoxia-relieving ability *in vivo*.

Subsequently, we looked into the *in vivo* antitumor efficacy of $Bi_2S_3$@Bi@PDA-HA/Art NRs. The tumor-bearing mice were randomly divided into seven groups ($n = 6$ per group) once the tumors reached ~100 $mm^3$: (1) PBS, (2) PBS + NIR, (3) $Bi_2S_3$@Bi@PDA-HA NRs, (4) Art, (5) $Bi_2S_3$@Bi@PDA-HA/Art NRs, (6) $Bi_2S_3$@Bi@PDA-HA NRs + NIR, (7) $Bi_2S_3$@Bi@PDA-HA/Art NRs + NIR. On Day 0, mice were injected with PBS, Art, $Bi_2S_3$@Bi@PDA-HA NRs, or $Bi_2S_3$@Bi@PDA-HA/Art NRs. For the NIR-involved groups, the mice were irradiated for 6 min in tumor regions with an 808 nm laser at a power density of 1.0 W/$cm^2$ after 8 h of injection. Compared to the control group, the body weight curves demonstrated no obvious changes in the experimental groups (Fig. 5B), implying that our nanoplatform was biocompatible. However, the tumor size of the PBS group increased rapidly throughout the study (Fig. 5C), while administration of Art and $Bi_2S_3$@Bi@PDA-HA/Art NRs reduced tumor growth with TGI values of 15.89% and 15.08%, respectively, due to the anti-cancer activity of Art. Although laser irradiation and $Bi_2S_3$@Bi@PDA-HA NRs had a negligible effect on tumor growth, their combination exhibited a moderate growth inhibition effect with a TGI of 61.18% because of the excellent photothermal performance and simultaneous $O_2$ and ROS production ability of $Bi_2S_3$@Bi@PDA-HA NRs. Furthermore, the tumor size was suppressed significantly in the $Bi_2S_3$@Bi@PDA-HA/Art NRs plus 808 nm laser irradiation group with a TGI value of 94.04% compared to other groups, highlighting the synergistic effect of the CDT, PTT, and Art assisted PDT. These findings were validated by the images of the collected distant tumors (Fig. 5D). Moreover, mice in the groups of $Bi_2S_3$@Bi@PDA-HA/Art NRs + NIR laser irradiation significantly prolonged survival lifetime compared to other groups (Fig. S25).

The H&E-stained tumor sections showed that the mice treated with $Bi_2S_3$@Bi@PDA-HA/Art NRs under laser irradiation induced the highest cell apoptosis and tumors ablation (Fig. 5E). Overall, our results confirmed that $Bi_2S_3$@Bi@PDA-HA/Art NRs could be considered as a suitable candidate for PTT/PDT/CDT synergistic therapy *in vivo*.

## 4. Conclusion

To conclude, a TME-responsive multifunctional therapeutic platform based on $Bi_2S_3$@Bi@PDA-HA/Art NRs was proposed for synergistic PDT/PTT/CDT. $Bi_2S_3$@Bi NRs with Z-scheme heterostructure enabled the nanoplatform with excellent photothermal performance as well as the ability to simultaneously produce $O_2$ and ROS production for improved hypoxic tumor phototherapy. The densely coated PDA/ABC and HA layers on the nanoplatform's surface not only increased the cancer-targeting efficiency but also induced the acidic TME/NIR-responsive "bomb-like" release of Art. Moreover, Art encapsulated in the nanoplatform could induce ferroptosis by consuming extracellular GSH and decreasing GPX4 levels to achieve efficient $H_2O_2$-independent CDT treatment, which significantly improved the PDT efficiency of $Bi_2S_3$@Bi NRs. The excellent antitumor activity and good biocompatibility endowed the multi-mode nanoplatforms with huge potential in clinical applications.

## Conflicts of interest

The authors declare that they have no known competing financial interests or personal relationships that could have appeared to influence the work reported in this paper.

## Acknowledgments

Financial support was provided by the National Natural Science Foundation of China (grant no. 21807024), the Youth Top-notch Talents Supporting Plan of Hebei Province (QNBJ19004), Scientific Research Foundation of Hebei Province for the Returned Overseas Chinese Scholars (C20220508), the Science and Technology Project of Hebei Education Department (no. ZD2021072), the Central Guidance on Local Science and Technology Development Fund of Hebei Province (226Z2601G) and Science Fun for Creative Research Groups of Natural Science Foundation of Hebei Province (no. H2020206474). This work was also supported by the Postdoctoral Fund of Hebei Medical University.

## Supplementary materials

Supplementary material associated with this article can be found, in the online version, at doi:10.1016/j.ajps.2023.100798.

## References

[1] Zhang M, Qina X, Xu W, Wang Y, Song Y, Garg S, et al. Engineering of a dual-modal phototherapeutic nanoplatform for single NIR laser-triggered tumor therapy. J Colloid Interface Sci 2021;594:493–501.
[2] Zhang J, Wang N, Li Q, Zhou Y, Luan Y. A two-pronged photodynamic nanodrug to prevent metastasis of basal-like breast cancer. Chem Commun 2021;57(18):2305–8.
[3] Zhou YX, Ren XM, Hou ZS, Wang NN, Jiang Y, Luan YX. Engineering a photosensitizer nanoplatform for amplified photodynamic immunotherapy via tumor microenvironment modulation. Nanoscale Horiz 2021;6(2):120–31.
[4] Wei F, Rees TW, Liao X, Ji L, Chao H. Oxygen self-sufficient photodynamic therapy. Coord Chem Rev 2021;432:213714.
[5] Li X, Kwon N, Guo T, Liu Z, Yoon J. Innovative strategies for hypoxic-tumor photodynamic therapy. Angew Chem Int Ed 2018;57(36):11522–31.
[6] Wang H, Li J, Wang Y, Gong X, Xu X, Wang J, et al. Nanoparticles-mediated reoxygenation strategy relieves tumor hypoxia for enhanced cancer therapy. J Control Release 2020;319:25–45.
[7] Wan Y, Fu LH, Li C, Lin J, Huang P. Conquering the hypoxia limitation for photodynamic therapy. Adv Mater 2021;33(48):2103978.
[8] Phua SZF, Yang G, Lim WQ, Verma A, Chen H, Thanabalu T, et al. Catalase-integrated hyaluronic acid as nanocarriers for enhanced photodynamic therapy in solid tumor. ACS Nano 2019;13(4):4742–51.
[9] Zeng W, Zhang H, Deng Y, Jiang A, Bao X, Guo M, et al. Dual-response oxygen-generating $MnO_2$ nanoparticles with polydopamine modification for combined photothermal-photodynamic therapy. Chem Eng J 2020;389:124494.

[10] Yang X, Liu R, Zhong Z, Huang H, Shao J, Xie X, et al. Platinum nanoenzyme functionalized black phosphorus nanosheets for photothermal and enhanced-photodynamic therapy. Chem Eng J 2021;409:127381.
[11] Dan Q, Hu D, Ge Y, Zhang S, Li S, Gao D, et al. Ultrasmall theranostic nanozymes to modulate tumor hypoxia for augmenting photodynamic therapy and radiotherapy. Biomater Sci 2020;8(3):973–87.
[12] Shen J, Yu H, Shu Y, Ma M, Chen H. A robust ROS generation strategy for enhanced chemodynamic/photodynamic therapy via $H_2O_2/O_2$ self-supply and $Ca^{2+}$ overloading. Adv Funct Mater 2021;31(50):2106106.
[13] Sang Y, Cao F, Li W, Zhang L, You Y, Deng Q, et al. Bioinspired construction of a nanozyme-based $H_2O_2$ homeostasis disruptor for intensive chemodynamic therapy. J Am Chem Soc 2020;142(11):5177–83.
[14] Li Y, Zhao P, Gong T, Wang H, Jiang X, Cheng H, et al. Redox dyshomeostasis strategy for hypoxic tumor therapy based on DNAzyme-loaded electrophilic ZIFs. Angew Chem Int Ed 2020;59(50):22537–43.
[15] Cheng Y, Zheng R, Wu X, Xu K, Song P, Wang Y, et al. Thylakoid membranes with unique photosystems used to simultaneously produce self-supplying oxygen and singlet oxygen for hypoxic tumor therapy. Adv Healthc Mater 2021;10(6):2001666.
[16] Li W, Fan Y, Lin J, Yu P, Wang Z, Ning C. Near-infrared light-activatable bismuth-based nanomaterials for antibacterial and antitumor treatment. Adv Healthc Mater 2022;5(9):2200027.
[17] Kang Y, Li Z, Yang Y, Su Z, Ji X, Zhang S. Antimonene nanosheets-based Z-scheme heterostructure with enhanced reactive oxygen species generation and photothermal conversion efficiency for photonic therapy of cancer. Adv Healthc Mater 2021;10(3):2001835.
[18] Cheng Y, Kong X, Chang Y, Feng Y, Zheng R, Wu X, et al. Spatiotemporally synchronous oxygen self-supply and reactive oxygen species production on Z-scheme heterostructures for hypoxic tumor therapy. Adv Mater 2020;32(11):1908109.
[19] Pan C, Ou M, Cheng Q, Zhou Y, Yu Y, Li Z, et al. Z-scheme heterojunction functionalized pyrite nanosheets for modulating tumor microenvironment and strengthening photo/chemodynamic therapeutic effects. Adv Funct Mater 2020;30(3):1906466.
[20] Li Z, Dai H, Huang X, Feng J, Deng J, Wang Z, et al. Artesunate synergizes with sorafenib to induce ferroptosis in hepatocellular carcinoma. Acta Pharmacol Sin 2021;42(2):301–10.
[21] Shao Y, Wang Z, Hao Y, Zhang X, Wang N, Chen K, et al. Cascade catalytic nanoplatform based on “butterfly effect” for enhanced immunotherapy. Adv Healthc Mater 2021;10(8):2002171.
[22] Li Z, Wu X, Wang W, Gai C, Zhang W, Li W, et al. Fe(II) and tannic acid-cloaked MOF as carrier of artemisinin for supply of ferrous ions to enhance treatment of triple-negative breast cancer. Nanoscale Res Lett 2021;16(1):1–11.
[23] Li B, Yang L, Peng X, Fan Q, Wei S, Yang S, et al. Emerging mechanisms and applications of ferroptosis in the treatment of resistant cancers. Biomed Pharmacother 2020;130:110710.
[24] Xu K, Cheng Y, Yan J, Feng Y, Zheng R, Wu X, et al. Polydopamine and ammonium bicarbonate coated and doxorubicin loaded hollow cerium oxide nanoparticles for synergistic tumor therapy. Nano Res 2019;12(12):2947–53.
[25] Choi KY, Han HS, Lee ES, Shin JM, Almquist BD, Lee DS, et al. Hyaluronic acid-based activatable nanomaterials for stimuli-responsive imaging and therapeutics: beyond CD44-mediated drug delivery. Adv Mater 2019;31(34):1803549.
[26] Faisal M, Rashed MA, Alhmami MAM, Harraz FA. Clean light oriented ultrafast $Pt/Bi_2S_3$ nanoflakes for the photocatalytic destruction of gemifloxacin mesylate drug and methylene blue. J Photochem Photobiol A: Chem 2021;414:113288.
[27] Xiong P, Bai P, Li A, Li B, Cheng M, Chen Y, et al. Bismuth nanoparticle@carbon composite anodes for ultralong cycle life and high-rate sodium-ion batteries. Adv Mater 2019;31(48):1904771.
[28] Wang J, Li L, Yu H, Guan F, Wang D. Binary-ternary $Bi_2S_3$-$AgBiS_2$ rod-to-rod transformation via anisotropic partial cation exchange reaction. Inorg Chem 2019;58(19):12998–3006.
[29] Cheng Y, Chen C, Hu S, Liu X, Zhang L, Huang W, et al. A facile photoelectrochemical sensor for high sensitive dopamine and ascorbic acid detection based on Bi surface plasmon resonance-promoted $BiVO_4$ microspheres. J Electrochem Soc 2020;167(2):027536.
[30] Wang S, Li X, Chen Y, Cai X, Yao H, Gao W, et al. A facile one-pot synthesis of a two-dimensional $MoS_2/Bi_2S_3$ composite theranostic nanosystem for multi-modality tumor imaging and therapy. Adv Mater 2015;27(17):2775–82.
[31] Gu JW, Guo RT, Miao YF, Liu YZ, Wu GL, Duan CP, et al. Noble-metal-free Bi/g-$C_3N_4$ nanohybrids for efficient photocatalytic $CO_2$ reduction under simulated irradiation. Energy Fuels 2021;35(12):10102–12.
[32] Li Q, Chen Y, Zhou X, Chen D, Li Y, Yang J, et al. Hyaluronic acid-methotrexate conjugates coated magnetic polydopamine nanoparticles for multimodal imaging-guided multistage targeted chemo-photothermal therapy. Mol Pharm 2018;15(9):4049–62.
[33] Shi JH, Wang TR, You YQ, Akhtar ML, Liu ZJ, Han F, et al. Enhancement of ultralow-intensity NIR light-triggered photodynamic therapy based on exo- and endogenous synergistic effects through combined glutathione-depletion chemotherapy. Nanoscale 2019;11:13078–88.
[34] He S, Krippes K, Ritz S, Chen Z, Best A, Butt HJ, et al. Ultralow-intensity near-infrared light induces drug delivery by upconverting nanoparticles. Chem Commun 2015;51:431–4.
[35] Yuan Z, Tao B, He Y, Liu J, Lin CH, Shen X, et al. Biocompatible $MoS_2$/PDA-RGD coating on titanium implant with antibacterial property via intrinsic ROS-independent oxidative stress and NIR irradiation. Biomaterials 2019;217:119290.
[36] Zhao R, Fu C, Wang Z, Pan M, Ma B, Yin Q, et al. A pH-responsive nanoparticle library with precise pH tunability by co-polymerization with non-ionizable monomers. Angew Chem 2022;134:e202200152.
[37] Zhao M, Wang J, Lei Z, Lu L, Wang S, Zhang H, et al. NIR-II pH sensor with a FRET adjustable transition point for in situ dynamic tumor microenvironment visualization. Angew Chem 2021;133(10):5151–5.
[38] Li ZJ, Dai HQ, Huang XW, Feng J, Deng JH, Wang ZX, et al. Artesunate synergizes with sorafenib to induce ferroptosis in hepatocellular carcinoma. Acta Pharmacol Sin 2021;42(2):301–10.
[39] Chen G, Benthani F, Wu J, Liang D, Bian Z, Jiang X. Artemisinin compounds sensitize cancer cells to ferroptosis by regulating iron homeostasis. Cell Death Dis 2020;27:242–54.
[40] Sun Q, Liu B, Wang Z, Feng L, Zhao R, Dong S, et al. $H_2O_2/O_2$ self-supplementing and GSH-depleting $Ca^{2+}$ nanogenerator with hyperthermia-triggered, TME-responsive capacities for combination cancer therapy. Chem Eng J 2021;425:131485.
[41] Fan Z, Jiang B, Zhu Q, Xiang S, Tu L, Yang Y, et al. Tumor-specific endogenous $Fe^{II}$-activated, MRI-guided self-targeting gadolinium-coordinated theranostic nanoplatforms for amplification of ROS and enhanced chemodynamic chemotherapy. ACS Appl Mater Inter 2020;12(13):14884–904.

[42] Qiu M, Wang D, Huang H, Yin T, Bao W, Zhang B, et al. A regioselectively oxidized 2D Bi/$BiO_x$ lateral nano-heterostructure for hypoxic photodynamic therapy. Adv Mater 2021;33(49):2102562.
[43] Girotti AW, Fahey JM. Upregulation of pro-tumor nitric oxide by anti-tumor photodynamic therapy. Biochem Pharmacol 2020;176:113750.
[44] Ma QL, Shen MO, Han N, Xu HZ, Peng XC, Li QR, et al. Chlorin e6 mediated photodynamic therapy triggers resistance through ATM-related DNA damage response in lung cancer cells. Photodiagnosis Photodyn Ther 2022;37:102645.
[45] Ali OM, Bekhit AA, Khattab SN, Helmy MW, Abdel-Ghany YS, Teleb M, et al. Synthesis of lactoferrin mesoporous silica nanoparticles for pemetrexed/ellagic acid synergistic breast cancer therapy. Colloids Surf B 2020;188:110824.
[46] Kim D, Jo G, Chae Y, Subramani S, Lee BY, Kim EJ, et al. Bioinspired Camellia japonica carbon dots with high near-infrared absorbance for efficient photothermal cancer therapy. Nanoscale 2021;13:14426.
[47] Wei Y, Wang Z, Yang J, Xu R, Deng H, Ma S, et al. Reactive oxygen species/photothermal therapy dual-triggered biomimetic gold nanocages nanoplatform for combination cancer therapy via ferroptosis and tumor-associated macrophage repolarization mechanism. J Colloid Interf Sci 2022;606:1950–65.